Physical Chemistry Chemical Physics

RSC Publishing

Journals Physical Chemistry Chemical Physics Contents List DOI: 10.1039/b614546a

Phys. Chem. Chem. Phys., 2007, **9**, 1347-1361 | DOI: 10.1039/b614546a | Paper

Particle size dependent adsorption and reaction kinetics on reduced and partially oxidized Pd nanoparticles†

T. Schalow, B. Brandt, D. E. Starr, M. Laurin, S. K. Shaikhutdinov, S. Schauermann, J. Libuda‡ * and H.-J. Freund

Fritz-Haber-Institut der Max-Planck-Gesellschaft, Faradayweg 4-6, 14195, Berlin, Germany

Received 5th October 2006, Accepted 15th December 2006

First published on the web 23rd January 2007

Combining scanning tunneling microscopy (STM), IR reflection absorption spectroscopy (IRAS) and molecular beam (MB) techniques, we have investigated particle size effects on a Pd/Fe_3O_4 model catalyst. We focus on the particle size dependence of (i) CO adsorption, (ii) oxygen adsorption and (iii) Pd nanoparticle oxidation/reduction. The model system, which is based on Pd nanoparticles supported on an ordered Fe_3O_4 film on Pt(111), is characterized in detail with respect to particle morphology, nucleation, growth and coalescence behavior of the Pd particles. Morphological changes upon stabilization by thermal treatment in oxygen atmosphere are also considered. The size of the Pd particles can be varied roughly between 1 and 100 nm. The growth and morphology of the Pd particles on the Fe_3O_4/Pt(111) film were characterized by STM and IRAS of adsorbed CO as a probe molecule. It was found that very small Pd particles on Fe_3O_4 show a strongly modified adsorption behavior, characterized by atypically weak CO adsorption and a characteristic CO stretching frequency around 2130 cm^{-1}. This modification is attributed to a strong interaction with the support. Additionally, the kinetics of CO adsorption was studied by sticking coefficient experiments as a function of particle size. For small particles it is shown that the CO adsorption rate is significantly enhanced by the capture zone effect. The absolute size of the capture zone was quantified on the basis of the STM and sticking coefficient data. Finally, oxygen adsorption was studied by means of MB CO titration experiments. Pure chemisorption of oxygen is observed at 400 K, whereas at 500 K partial oxidation of the particles occurs. The oxidation behavior reveals strong kinetic hindrances to oxidation for larger particles, whereas facile oxidation and reduction are observed for smaller particles. For the latter, estimates point to the formation of oxide layers which, on average, are thicker than the surface oxides on corresponding single crystal surfaces.

1. Introduction

The selectivity and activity of supported catalysts are often found to be strongly dependent on the surface structure, particle morphology and size, on the support and on the presence of promoters and poisons.[1,2] Especially, the particle size is a critical issue, as it determines not only the density of active sites but is also related to changes in the electronic and geometric structure as well as to interactions with the support.

A particular complication arises in case of metal nanoparticles in oxidative environments. Often the interaction of oxygen with metal surfaces and, particularly, with small metal particles turns out to be rather complex. There is an ongoing discussion on the nature of the different oxygen and oxide phases and on their activity with respect to catalytic reactions (see *e.g.*ref. 3–7). A large number of experimental and theoretical studies focused on Pd surfaces, trying to identify different chemisorbed oxygen phases, subsurface oxygen species, surface and bulk oxides[6–26] Still, the role of this species in

catalytic reactions is only poorly understood and some controversy remains.[5,27,28]

In the case of supported metal nanoparticles the situation becomes further intricate, as oxidation behavior, particle size and interaction with the support turn out to be closely related. For Pd nanoparticles supported on an ordered Fe_3O_4 film on Pt(111), we have recently shown that thin Pd oxide layers formed during oxygen exposure are strongly stabilized at the particle/support interface, leading to the preferential oxidation of the interface region.[6,7,23–25] Also, oxidation was found to be closely related to particle sintering.[24] Moreover, the average oxidation state of the Pd particles, which dynamically changes as a function of the reactant environment, was shown to control the catalytic activity of the particles.[7] Finally, the oxidation behavior was found to be strongly size dependent.[25] Whereas very small particles tend to get oxidized completely, larger particles show strong kinetic hindrances with respect to interface and surface oxide formation.

In this contribution we present a comprehensive study on the adsorption and reaction kinetics on Pd/Fe_3O_4 as a function of particle size, using CO adsorption and oxidation as a test reaction. We consider both, metallic and partially oxidized particles. It is noteworthy that we were capable of varying the size of the Pd aggregates by nearly two orders of magnitude. The large variation in size allows us to study individual effects in the adsorption and reaction kinetics which otherwise could not be clearly identified. This kinetic information is obtained by combining structural data from scanning tunneling microscopy (STM) with molecular beam (MB) techniques[29–32] and IR reflection absorption spectroscopy (IRAS) (see *e.g.*ref. 32 and 33).

2. Experimental

All molecular beam (MB) experiments were performed in a UHV apparatus at the Fritz-Haber-Institut (Berlin), which has been described recently. The system offers the experimental possibility of crossing up to three molecular beams on the sample surface.[34]

Two effusive beams are generated by doubly differentially pumped sources based on multi-channel arrays. These beams are modulated using remote-controlled shutters and valves. Both sources were operated at room temperature. The beam diameters were chosen such that they exceed the sample diameter. All experiments have been performed using high purity O_2 (Linde, 99.999%) and CO (Linde, 99.997% further purified by a gas filter (Mykrolis)). Typical intensities of the beams were 2.1×10^{14} molecules cm^{-2} s^{-1} corresponding to an effective pressure on the sample of 8×10^{-7} mbar. The third beam is a supersonic beam, generated by a triply differentially pumped source from a supersonic expansion. It is modulated by a solenoid valve and a remote-controlled shutter. In this study, the supersonic source was used to generate $^{18}O_2$ beams (Campro Scientific, 95% ^{18}O, 99.7% purity) at an intensity of 4.6×10^{14} molecules cm^{-2} s^{-} and CO beams at an intensity of 2.3×10^{13} molecules cm^{-2} s^{-1} for the sticking coefficient measurements (typical backing pressures 1.0–1.2 bar). The diameter of the supersonic beam was chosen smaller than the sample for the sticking coefficient measurements.

For gas-phase detection an automated quadrupole mass spectrometer (QMS) system (ABB Extrel) was employed, detecting the partial pressure of the reactants and the product. All QMS data have been checked and/or corrected with respect to blind experiments using catalytically inert sample surfaces. In addition, the MB apparatus allows us to acquire IR spectra (IRAS, IR reflection absorption spectroscopy) during gas exposure and reaction using a vacuum FT-IR spectrometer (Bruker IFS 66v). In addition to the IR spectra shown in the following, IR spectroscopy was used as a spectroscopic tool in order to control the reproducibility and stability of the model surfaces prepared. All IR spectra were acquired with a spectral resolution of 2 cm^{-1}, and an MIR polarizer to select the p-component of the IR light only.

Scanning tunneling microscopy measurements were performed in a separate UHV chamber (at a base pressure of $<2 \times 10^{-10}$ mbar) equipped with Auger electron spectroscopy/low energy electron diffraction (AES/LEED) (Specs), a quadrupole mass spectrometer (QMS) (Fisons VG) and an STM (Micro H, Omicron) along with standard sample cleaning and preparation facilities. All images were recorded using commercial Pt/Ir tips (LOT-Oriel GmbH) with tunneling currents of approx. 0.7 nA and positive sample biases of approx. 1.4 V.

The Pd/Fe_3O_4 model catalyst was prepared as follows: The thin (~100 Å) Fe_3O_4 film was grown on Pt(111) by repeated cycles of Fe (>99.99%, Goodfellow) deposition and subsequent oxidation (see ref. 35 and 36 for details). Cleanliness and quality of the oxide film was checked by IRAS of adsorbed CO and LEED. Pd particles (>99.9%, Goodfellow) were grown by physical vapor deposition using a commercial evaporator (Focus, EFM 3, flux calibrated by a quartz microbalance). Pd coverages between 7×10^{13} atoms cm^{-2} and 1.3×10^{16} atoms cm^{-2} (nominal thickness 0.1 to 20 Å: 1 Å corresponds to 7×10^{14} atoms cm^{-2}) were deposited at a sample temperature of 115 K (typical deposition rates: 2.7×10^{14} atoms cm^{-2} min^{-1}). During Pd evaporation the sample was biased in order to avoid creation of defects by metal ions. Directly after Pd deposition, the sample was annealed to 600 K and was stabilized by several cycles of oxygen (8×10^{-7} mbar for 1000 s) and CO exposure (8×10^{-7} mbar for 3000 s) at 500 K (compare *e.g.* ref. 24, 35, and 36).

3. Results and discussion

3.1 Particle growth and stabilization in oxygen atmosphere

As a critical prerequisite for the particle size-dependent investigations, we consider nucleation and growth behavior of the particles first. The Pd model catalysts were prepared by physical vapor deposition (PVD) of different amounts of Pd (nominal thicknesses 0.3 to 15 Å) onto a thin and well-ordered Fe_3O_4 film grown on Pt(111)[35] under ultrahigh vacuum (UHV) conditions. After deposition at 115 K the sample was annealed to 600 K and STM images were taken. In Fig. 1 (left column), a series of corresponding images is show as a function of the nominal Pd thickness. At lowest Pd coverage (0.3 Å) nucleation of the Pd particles occurs in a well-distributed fashion over the Fe_3O_4 terraces. The inset shows a close-up of a few individual particles. The particles appear round and no regular crystalline shape can be identified. However, it should be kept in mind that due to convolution with the tip shape, the identification of particle shapes is difficult in the low particle size limit (compare *e.g.* ref. 37).

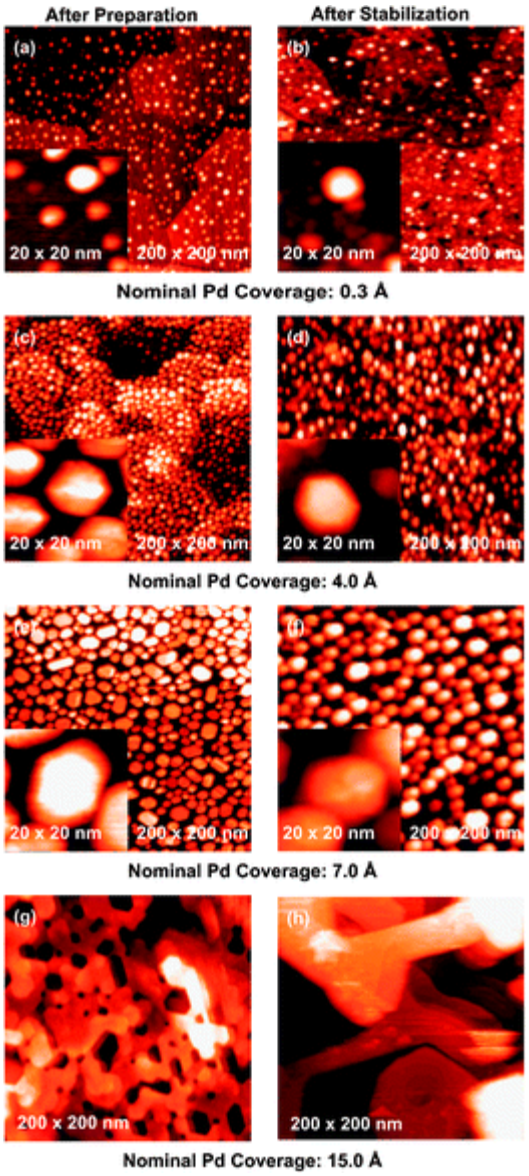

Fig. 1 STM images of the Pd/Fe_3O_4 model catalyst as a function of Pd coverage before and after stabilization.

With increasing metal coverage there is further nucleation of Pd particles up to nominal Pd coverages of about 4 Å. Here, a maximum particle number density of up to 3.8×10^{12} particles cm^{-2} is reached. The close-up shows the formation of crystalline aggregates with a rather flat top of near hexagonal shape. This indicates that the Pd particles grow in (111) orientation, with their sides being terminated by (111) and (100) facets. If we proceed to even higher nominal Pd coverage (7 Å), the particle number density decreases again. This decrease is due to the onset of coalescence, as indicated for example by the formation of some larger elongated crystallites (Fig. 1e). If we finally consider even higher metal coverages, the particle film is found to transform into an interconnected Pd structure as a result of strong coalescence. Even in this range, however, the hexagonal shape of the Pd areas is clearly visible, indicating growth of a (111)-oriented thin film.

In a previous publication we have shown that strong restructuring of the Pd particles occurs upon annealing in an oxygen containing environment.[24] Specifically, it was demonstrated that particle restructuring and sintering is directly connected to the onset of oxidation and, in particular, to the formation of surface and interface oxides. Thus, the Pd deposit prepared in UHV under oxygen-free conditions must be stabilized by repeated oxidation reduction cycles before they show a constant activity in kinetic studies. Therefore the Pd model catalysts were treated several times with oxygen (2.1×10^{14} molecules cm^{-2} s^{-1}, 1000 s, 600 L) and CO (2.1×10^{14} molecules cm^{-2} s^{-1}, 3000 s, 1800 L) at 500 K.

STM images of the stabilized model systems are shown in Fig. 1 (right column). For all Pd coverages it is found that the particle number density decreases drastically upon stabilization and, simultaneously, the particle size increases. Typically, the Pd particles show a well-defined crystalline shape after the stabilization procedure, again exposing a planar nearly hexagonal top (indicating (111) orientation). Measurements of the top facet size and the particle height reveal that the particles are rather flat (the size of the flat top facet can be determined with good accuracy in STM). In the intermediate coverage regime an aspect ratio (height : diameter) of approximately 1 : 3.5 is determined. The flat shape hints to a relatively strong interaction with the support (compare *e.g.*ref. 38 and 39 and references therein). From the information on the particle shape, we can estimate the fraction of (111) facets to about 80% and the fraction of (100) facets to about 20%. At nominal Pd coverages above 7 Å coalescence leads to the formation of very large ordered and (111)-oriented Pd structures on a characteristic length scale of 50 to 100 Å. A summary of the structural data derived from STM is given in Table 1.

Table 1 Growth parameters and structural data of the Pd/Fe_3O_4 model catalyst as determined from STM (see Fig. 2)

Nominal Pd coverage	0.3 Å	4.0 Å	7.0 Å	15.0 Å
Nominal Pd coverage (atoms cm^{-2})	2.0×10^{14}	2.7×10^{15}	4.7×10^{15}	1.0×10^{16}
After annealing at 600 K				
Island density (cm^{-2})	1.7×10^{12}	3.8×10^{12}	1.0×10^{12}	—
Number of Pd atoms/island	~100	~700	~4900	—
Average size/nm	**~2**	**~4**	**~8**	**~15**
After stabilization				
Island density (cm^{-2})	4.8×10^{11}	8.4×10^{11}	6.0×10^{11}	—
Number of Pd atoms/island	~400	~3300	~8100	—
Average size/nm	**~4**	**~7**	**~12**	**~70**

For the size dependent studies it is desirable to extract quantitative information on the particle size and density from the STM data. Here, it should be kept in mind that the most reliable information from STM is the particle number density (see Fig. 2b), whereas it is difficult to extract exact particle diameters, at least for small particles. We have, therefore, estimated the particle diameter from the nominal Pd coverage and the particle number density. The particle number density as a function of nominal Pd coverage was estimated from STM experiments by linear interpolation or extrapolation. The average particle volume was derived by assuming a constant particle shape described by a half spheroid with an aspect ratio of 3.5. On the basis of these assumptions we obtain an estimate of the particle diameter as a function of the nominal Pd thickness. For very large nominal Pd coverages (>10.0 Å), an island density of the Pd aggregates could not be determined due to their interconnected structure. Therefore the average particle size in this regime was estimated by linearly extrapolating the size of the structures determined directly from the STM image for a nominal Pd coverage of 15.0 Å. The results of the corresponding estimates before and after stabilization treatment are displayed in Fig. 2a. In general, the curves show a behavior which is qualitatively expected on the basis of the STM data. The region of lower Pd thickness (up to approx. 5 Å) is dominated by particle nucleation and growth. At higher coverage the particle size increases rapidly due to the onset of coalescence. We will use the structural data from Fig. 2 and Table 1 in the following discussion of the size dependent adsorption and reaction behavior.

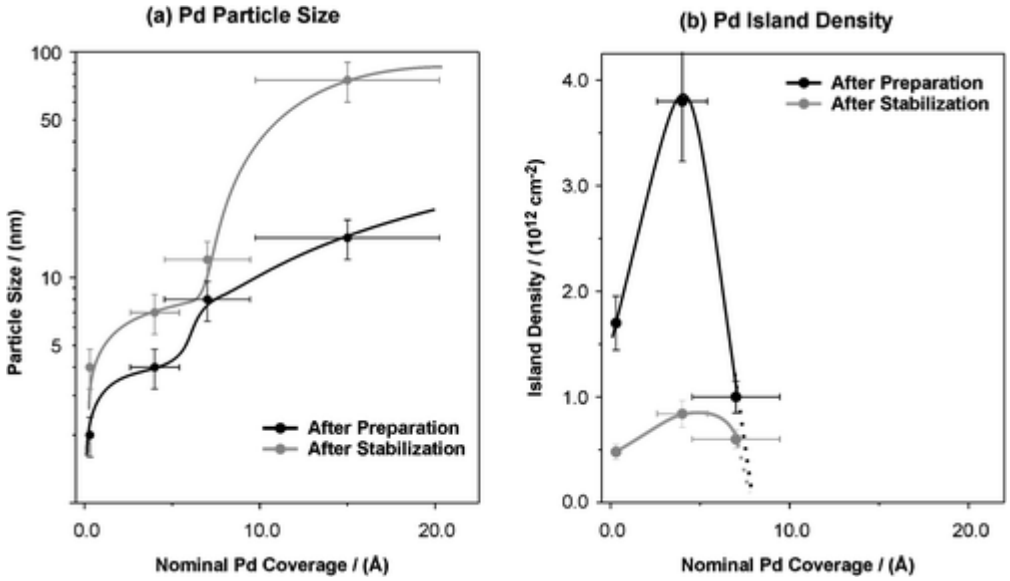

Fig. 2 Particle size and density of the Pd particles on Fe_3O_4 as estimated from STM (see text).

3.2 Size dependent adsorption behavior and stabilization procedure (IRAS)

In the following we monitor the particle growth and morphological changes upon stabilization (oxidation/reduction cycles) *via* IR spectroscopy of adsorbed CO.

Briefly, the CO adsorption behavior on Pd(111) and Pd(100) single crystals and on supported Pd particles can be summarized as follows: On Pd(111) fcc threefold hollow sites are occupied at low coverages, finally leading to a ($\sqrt{3} \times \sqrt{3}$)R30° superstructure at θ = 0.33.[40–47] In the low coverage limit, adsorbed CO on fcc hollow sites gives rise to an absorption band at 1808 cm^{-1}, shifting to higher frequencies with increasing coverage (1855 cm^{-1} at θ = 0.33). At higher coverage, site occupation was found to depend on adsorption conditions.[46,47] At a coverage of θ = 0.5 a c(4 × 2)-2CO structure is observed giving rise to a single absorption band around 1920 to 1930 cm^{-1}. Based on theoretical calculations and experiments, the structure was attributed to CO occupying a combination of fcc and hcp hollow sites.[44–46] More recent studies by STM and high-resolution PES (photoelectron spectroscopy) suggested that structures with CO occupying bridge sites compete with adsorption on hollow sites.[46,47] Occupation of bridge sites around θ = 0.6 has been found to give rise to absorption bands between 1955 cm^{-1} and 1970 cm^{-1}.[48–51] Saturation coverage at 100 K corresponds to a (2 × 2)-3CO superstructure at θ = 0.75 with characteristic vibrational bands at 1895 and 2110 cm^{-1}, in which hollow and on top sites are occupied.[46–49]

On Pd(100) the situation is simpler with bridge sites being occupied from low coverage to the c(2 × 2)-2CO superstructure at saturation coverage of θ = 0.5. With increasing coverage the vibrational band shows a large blue shift from 1895 to 1997 cm^{-1}.[41,52]

The absorption behaviour on Pd nanoparticles has been studied in detail and characteristic differences have been found with respect to the single crystal data.[37,53–58] First, adsorption of CO on on-top sites has been observed at temperatures of 300 K and below, giving rise to absorption bands in the region from 2070 and 2110 cm^{-1}. The exact positions of these bands depend on particle size and coverage. Typically, the fraction of on-top CO, which is relatively weakly bound, increases with decreasing particle size.[37,54] A second difference is related to the occupation of bridge sites. The corresponding bands are typically observed to dominate on Pd nanoparticles.[37,57] Adsorption of CO at bridge sites on particle edges gives rise to an intense absorption band, typically between 1970 and 2000 cm^{-1} (with the exact position depending on adsorption temperature, coverage and particle size).[58] CO adsorbed on hollow sites gives rise to the shoulders and bands at lower wavenumbers.

For all IRAS studies, it should be noted, however, that the intensity of the various bands cannot be easily related to the abundance of the corresponding species. This is due to strong dipole coupling

effects in the adsorbate layer as well as to possible differences in the dynamic dipole moment.[41,59,60] Therefore, we restrict ourselves to qualitative interpretation of the CO IR spectra in the following discussion.

Based on the above information we consider the IR reflection absorption spectra taken after exposure to CO (18 L, T = 125 K) before (Fig. 3, black traces) and after stabilization (Fig. 3 grey traces).

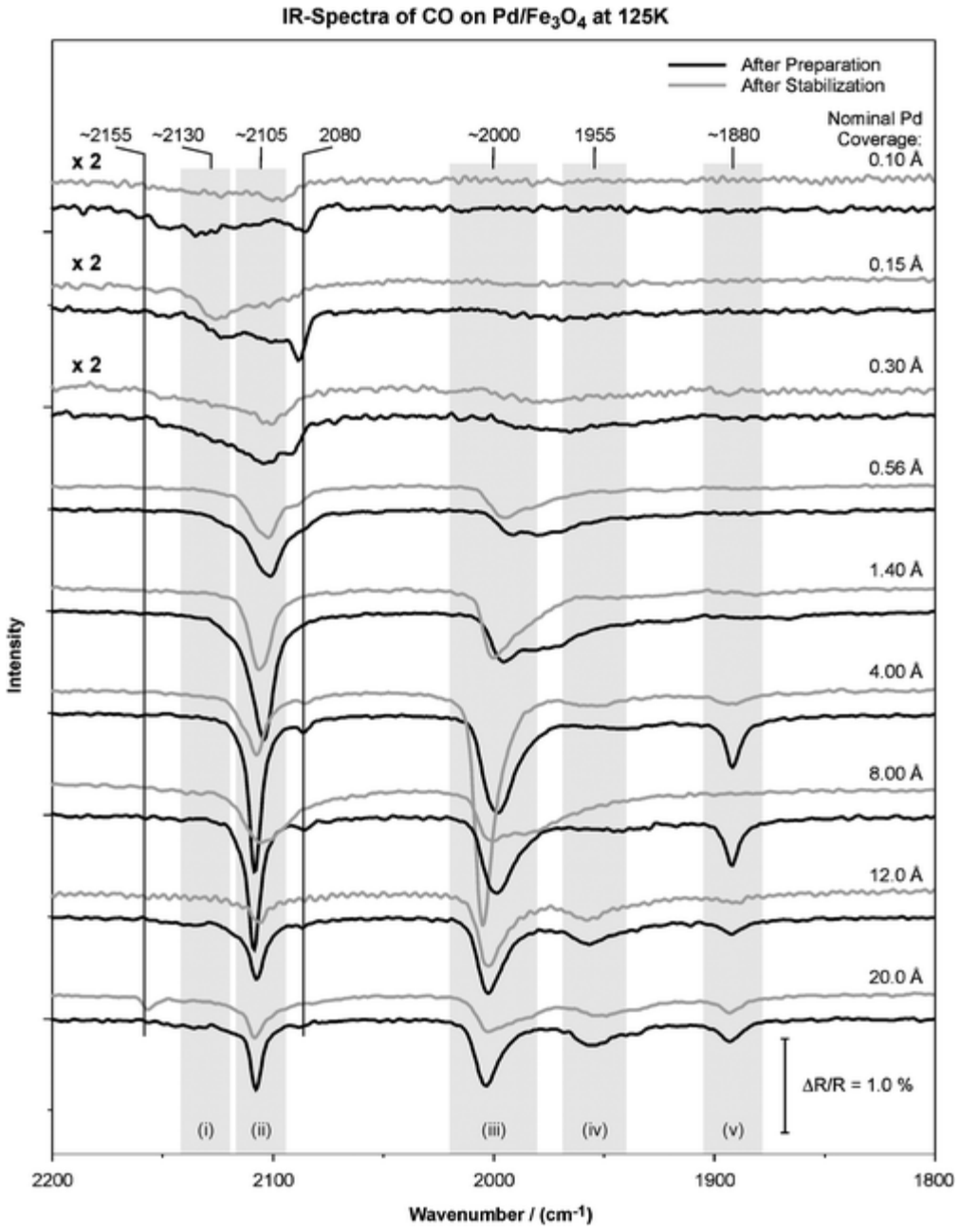

Fig. 3 IR reflection absorption spectra of the Pd/Fe_3O_4 model catalyst at 125 K before and after stabilization showing the CO stretching frequency region after CO saturation.

We focus on the range of low Pd coverage first (0.1 to 0.3 Å nominal Pd coverage). Here we observe bands at frequencies of approximately 2080, 2105 and 2130 cm^{-1}. The band at 2080 cm^{-1} contains contributions due to CO adsorption on the Fe_3O_4 film and on the Pd particles. The feature at 2105 cm^{-1} can be assigned to CO at on-top sites on small Pd aggregates. The band at 2105 cm^{-1} increases in intensity with increasing Pd coverage and represents the regular on-top species. The CO/Pd contribution to the band at 2080 cm^{-1} may be tentatively assigned to very small Pd aggregates or to specific defect sites.

Two points are noteworthy in connection with the IR spectra at low Pd coverage. First, there is a new band at 2130 cm^{-1}, which is not observed on single crystal surfaces. However, CO stretching frequencies in this range are typically found for co-adsorption of CO and O (see references and discussion in ref. 6, 24 and 61). Therefore, it appears plausible to assign this band, which is strongest at very low Pd coverage, to CO adsorption on Pd particles in close contact with the oxide support or Pd atoms at the particle/oxide interface. The second point concerns the adsorption at higher coordinated sites. In contrast to previous studies on Pd/Al_2O_3, no CO adsorbed in bridge or hollow sites is observed in the low coverage limit.[37,57] Both observations indicate that the interaction of Pd with the Fe_3O_4 support is substantially stronger than, for example, with Al_2O_3 supports, leading to pronounced modifications of the adsorption behaviour in the small particle limit.

Upon stabilization (oxidation/reduction cycles) the CO signals generally decrease, indicating a reduction of the adsorption capacity. A possible explanation is sintering of the particles. However, the spectra after stabilization do not resemble the spectra for larger particles. In fact the lower frequency bands which are characteristic of CO adsorption on larger Pd particles are decreasing rather than increasing. This observation suggests that the metal/oxide interaction is to a certain extent enhanced by the stabilization procedure.

Next we consider the intermediate coverage regime (0.56 to 4 Å nominal Pd coverage). In this region the spectra are comparable to those observed for Pd/Al_2O_3, previously.[37,57] The band around 2100 and 2000 cm^{-1} dominate the spectra. In addition, there is a weaker band at 1880 cm^{-1} and a weak diffuse band around 1930 cm^{-1}.

The dominant on-top peak around 2100 cm^{-1} is characteristic of CO adsorption at low temperature on small to medium sized particles and can be assigned to on-top CO adsorbed on Pd(111) facets and on-top CO at defect sites such as *e.g.* steps and edges. The strong peaks around 1970–2000 cm^{-1} can be attributed to bridge bonded CO at particle edge sites and Pd(100) facets. Intensity in the range between 1930 and 1960 cm^{-1} may be attributed to CO on hollow and bridge sites on (111) facets and the peak around 1880 cm^{-1} may at least partially be assigned to CO on hollow sites on (111) facets.

Upon stabilization the band in the on-top region decreases in intensity. This effect can be rationalized by oxygen induced sintering (compare *e.g.* ref. 24) and an ordering of the particles which leads to a lower density of edge and defect sites and, therefore, reduces on-top adsorption. This interpretation is consistent with the sharpening and blue-shift of the band in the region of bridge-bonded CO. Especially for deposition of 4 Å Pd, this band becomes very intense, indicating a large dynamic dipole for CO adsorbed on particle edges as well as strong dipole coupling effects leading to intensity transfer from the bands at lower frequency.[59] It is noteworthy that the CO band at 1880 cm^{-1}, which is mainly attributed to hollow bonded CO on Pd(111), decreases upon stabilization. This may partially be explained by a decrease in the fraction of (111) facets in favor of (100) facets, similar to the reshaping in oxygen atmosphere observed by Henry and coworkers.[39] The STM investigation discussed before (see section 3.1) shows, however, that also after stabilization the particle surface is clearly dominated by (111) facets. Therefore, the decrease in the hollow band may rather be related to changes in the site occupation of the facets due to the influence of edges and defects as well as to intensity transfer effects.

Finally, we consider large Pd coverages (8–20 Å) corresponding to the regime of particle coalescence. Here, the Pd surface is dominated by extended interconnected aggregates exposing predominately large (111) facets. The CO IR spectra show the corresponding features, which are characteristic of CO adsorption on Pd(111). Coexistence of on-top and hollow CO is indicated by the two bands at 2110 and 1890 cm^{-1}. A band at 1955 cm^{-1} indicates CO at bridge sites on Pd(111). Finally, the band at approximately 2000 cm^{-1} contains contributions from bridge bound CO at particle edges and on Pd(100) sites. Upon stabilization the band intensity decreases, indicating a loss of Pd surface area. However, no qualitative changes in the spectra are apparent (disregarding the case of 8 Å Pd coverage, which is right at the onset of the coalescence regime and may involve extended mass transfer effects upon stabilization).

In order to obtain further insight into the size dependent CO adsorption behaviour, we have performed further adsorption experiments at T = 300 K. In Fig. 4a comparison is shown between the IR

spectra taken at 125 and 300 K. Here, we focus on the stabilized Pd particles only. It is noteworthy that at nominal Pd coverages below 0.3 Å, almost no CO absorption band can be detected at 300 K. In order to illustrate this peculiar behaviour, the integral absorption of all bands in the CO stretching frequency region is plotted as a function of the nominal Pd coverage in Fig. 4b. Atypically low adsorption capacities are observed at low Pd coverage, which do not reflect the changes in the Pd surface area. This behaviour is in sharp contrast to the adsorption of CO on Pd/Al_2O_3[54,62,63] and on Pd/MgO.[64–66] In spite of the majority of relatively weakly bound CO at high coverage, in these studies strongly bound CO was found down to low particle size, even showing adsorption energies exceeding the values on the Pd(111) single crystal surface. We attribute the unusual CO behavior on the Pd/Fe_3O_4 to a strong metal/oxide interaction, which leads to a modification of the adsorption properties of the Pd particles. As a result, CO occupies weakly binding on top sites with modified adsorption properties (as reflected by the shift in the CO stretching frequency to 2130 cm^{-1}). At larger nominal Pd coverage a characteristic band appears at 1953 cm^{-1}, which shifts to 1973 cm^{-1} with increasing particle size. This band is assigned to bridge bonded CO adsorbed at particle edges and (100) facets. The blue shift with increasing particle size is attributed to the increasing number of corresponding sites leading to an increasing dipole coupling. At intermediate particle sizes a shoulder around 1930 cm^{-1} appears, which transforms into the dominating feature at largest particle size. This peak is characteristic of CO on Pd(111) facets (see above) and reflects the dominance of large (111) facets in this case.

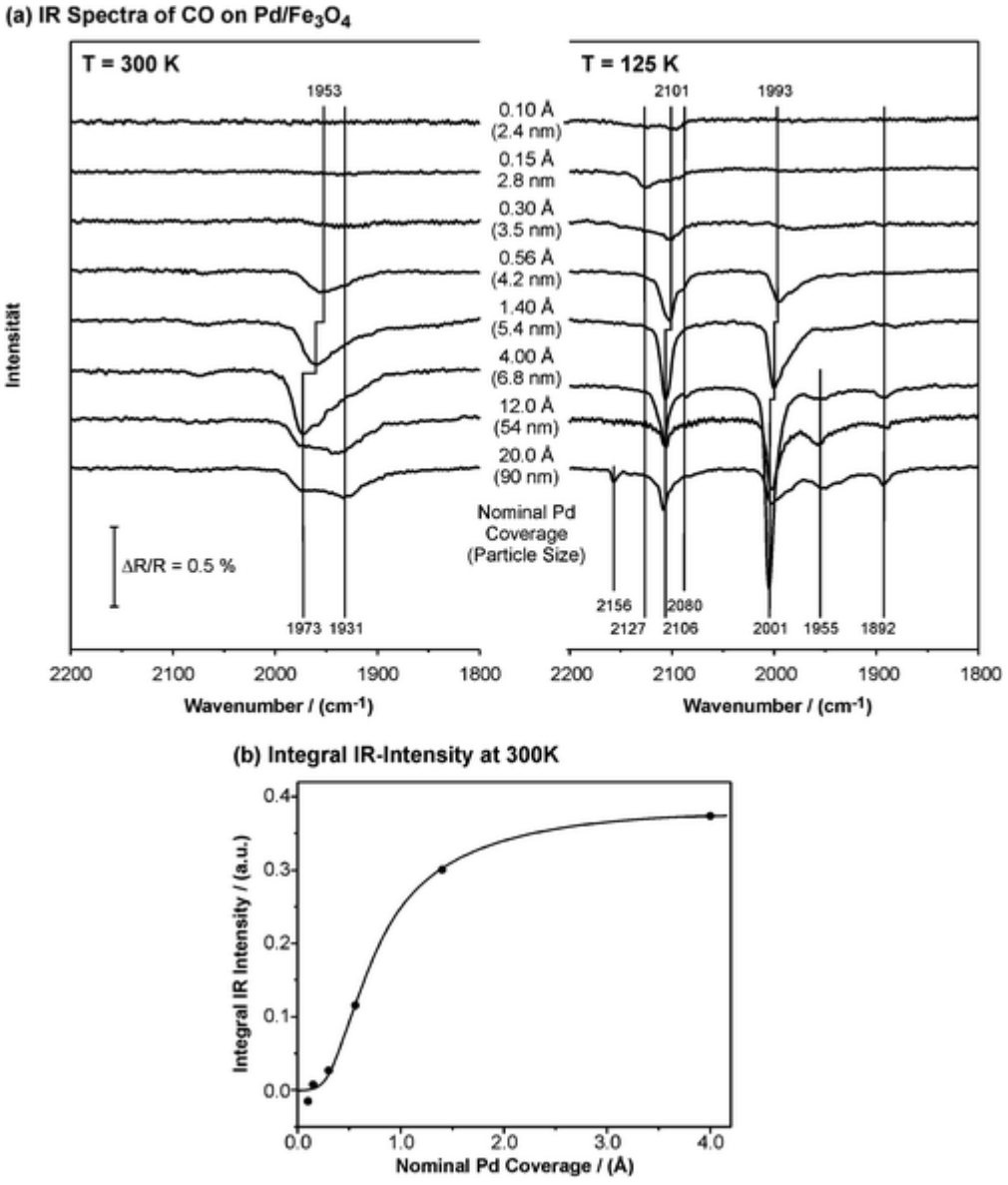

Fig. 4 (a) IR reflection absorption spectra of the Pd/Fe_3O_4 model catalyst at 125 and 300 K after stabilization showing the CO stretching frequency

region after CO saturation; (b) integral absorption in the CO stretching frequency region at 300 K.

3.3 Size dependent CO adsorption kinetics (molecular beam experiments)

In the next step we investigate the CO adsorption kinetics on Pd/Fe_3O_4 as a function of particle size. Therefore we perform King and Wells type[67,68] sticking coefficient measurements at 300 K. At this temperature, CO does not adsorb on the Fe_3O_4 support, but on the Pd particles only. The sticking coefficient experiments for the stabilized model surfaces are shown in Fig. 5. Corresponding measurements were also performed before stabilization.

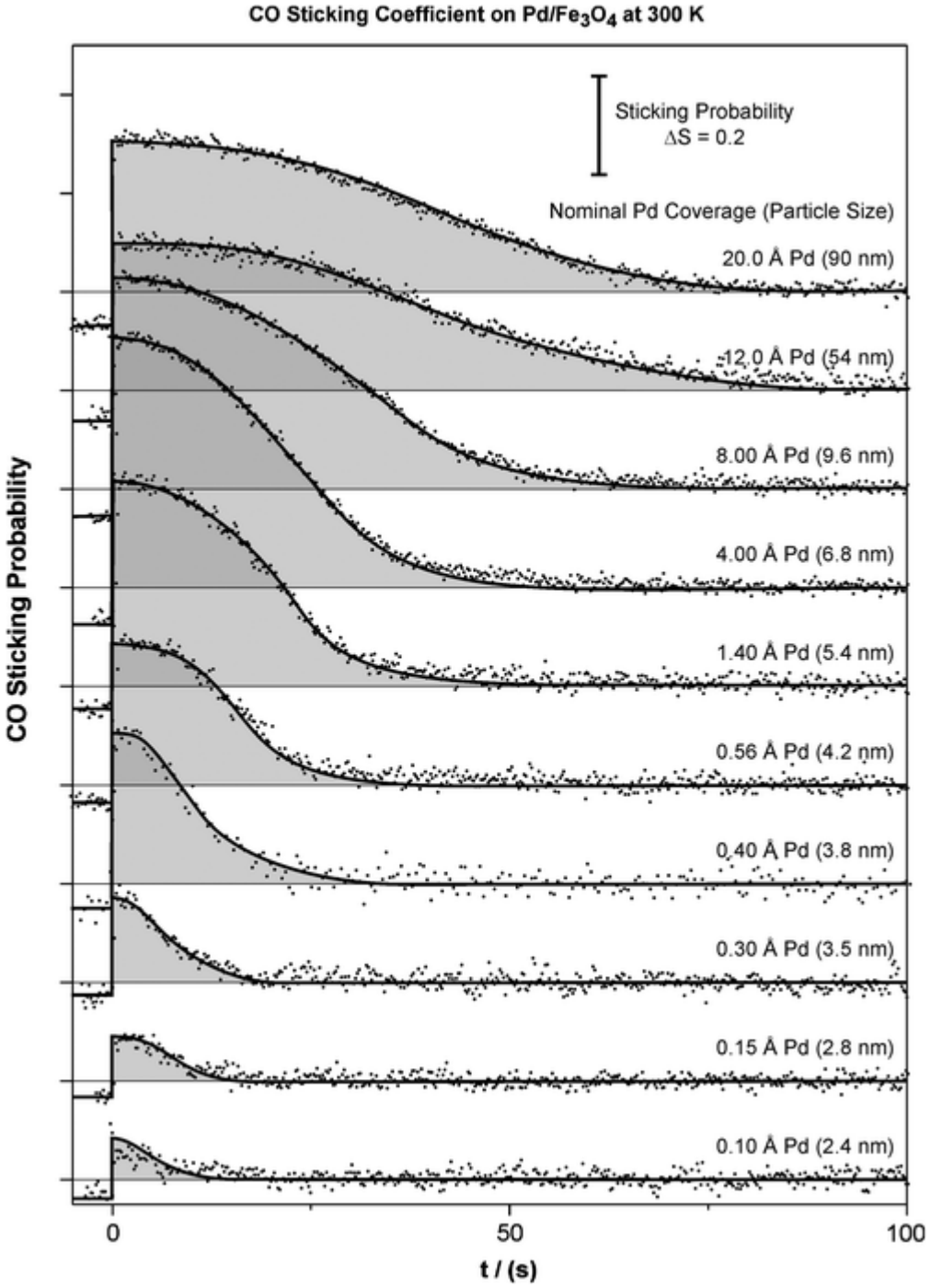

Fig. 5 CO sticking coefficient measurements on the stabilized Pd/Fe_3O_4 model catalyst at 300 K.

It is found that the characteristics of the CO sticking coefficient curves—including the shape of the

curve, the initial sticking coefficient, the adsorption capacity and the saturation exposure—strongly depend on the nominal Pd coverage. We will discuss these points in detail in the following.

First, it is apparent that the general adsorption mechanism follows a typical precursor type behavior for all particle sizes. This is expected, taking into account the coverage dependent CO sticking coefficient on Pd single crystal surfaces (compare *e.g.*ref. 69). The exact shape of the sticking coefficient curve depends on the nominal Pd coverage and is discussed below.

As a first piece of specific information we consider the total CO adsorption capacity of the Pd particles before and after stabilization. A corresponding graph is shown in Fig. 6a. It is found that the total CO adsorption capacity rapidly increases with increasing particle size in the low Pd coverage regime, but with increasing coverage approaches a limit of about 4.5×10^{14} molecules cm^{-2} at a nominal Pd coverage of ~4 Å. At even higher coverage, the CO adsorption capacity slightly decreases. In line with the STM data (see section 3.1) the region of increasing adsorption capacity can be attributed to the regime of nucleation and growth, whereas in the region of constant or even decreasing adsorption capacity coalescence of Pd particle dominates. The adsorption capacity after stabilization shows the same qualitative behavior as before, but the absolute adsorption capacity decreases substantially. Naturally, this effect can be attributed to the increasing particle size and decreasing particle number density upon stabilization.

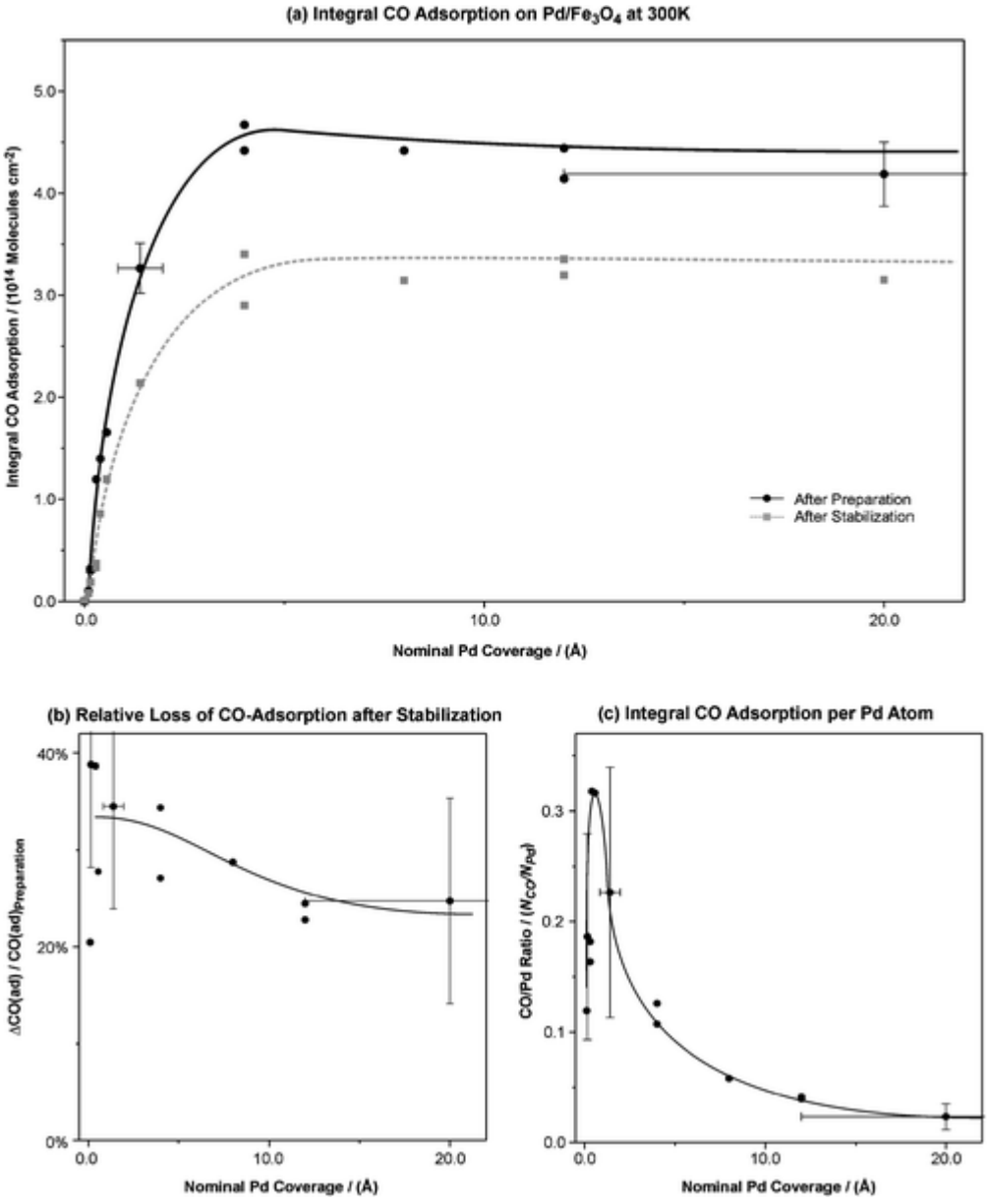

Fig. 6 (a) Integral CO adsorption capacity of the Pd/Fe_3O_4 model catalyst at 300 K as determined from the sticking coefficient measurements (see

Fig. 6); (b) relative loss of CO adsorption capacity upon stabilization; (c) CO adsorption capacity per Pd atom.

A somewhat surprising behavior is observed in the limit of very small Pd coverage. Here, the adsorption capacity shows an s-like shape, with an atypically low adsorption capacity. The effect becomes more obvious if we plot the CO adsorption capacity per deposited Pd atom at CO saturation (see Fig. 6c). Because of the decreasing Pd dispersion of the model catalyst with increasing nominal Pd coverage (*i.e.* increasing average particle size) one would expect a monotonously decreasing CO/Pd ratio, if the adsorption properties of the surface Pd atoms were independent of particle size. Indeed we find the expected monotonous decrease for larger nominal coverages (approximately >1 Å). For smaller Pd coverage the CO adsorption capacity per Pd atom is, however, found to decrease with decreasing particle size (in spite of the large error bars at low Pd coverage the effect is well reproducible and can, therefore, be considered to be significant). This decrease cannot be explained on the basis of the growth behavior only, as the Pd dispersion is expected to increase monotonously with decreasing particle size. Therefore, the decreasing CO adsorption capacity in the limit of small particle sizes must be attributed to a change in adsorption behavior itself. We associate the low CO coverage with a modification of the adsorption properties due to interactions with the oxide support. As a result, CO adsorption apparently becomes very weak for small Pd particles and CO is not adsorbed permanently at 300 K. This observation is consistent with the IRAS studies discussed in section 3.2, indicating that for small particles a strong metal/oxide interaction leads to modification of the adsorption properties and weak CO bonding at on-top sites only. The sticking coefficient measurements, however, clearly prove the decrease in adsorption capacity, whereas no quantitative information on coverage is available from the IRAS studies.

After stabilization the CO adsorption capacity decreases significantly due to particle sintering and ordering. The relative loss in adsorption capacity upon stabilization is plotted in Fig. 6b. It is found that the loss is largest for small Pd particles (approximately 35%) and decreases to approximately 20% for the largest particles. This behavior is expected to take into account the lower stability of small aggregates which, for kinetic and thermodynamic reasons, are more prone to sintering processes.

As a second piece of information we consider the CO sticking coefficient as a function of particle size. A detailed comparison of three sticking coefficient curves at low, intermediate and high Pd coverage is given in Fig. 7. It is observed that from low to intermediate Pd coverages the initial sticking coefficient and the exposure required for CO saturation increase. If we proceed from intermediate to high Pd coverage the saturation exposure still increases, but the initial sticking coefficient decreases again.

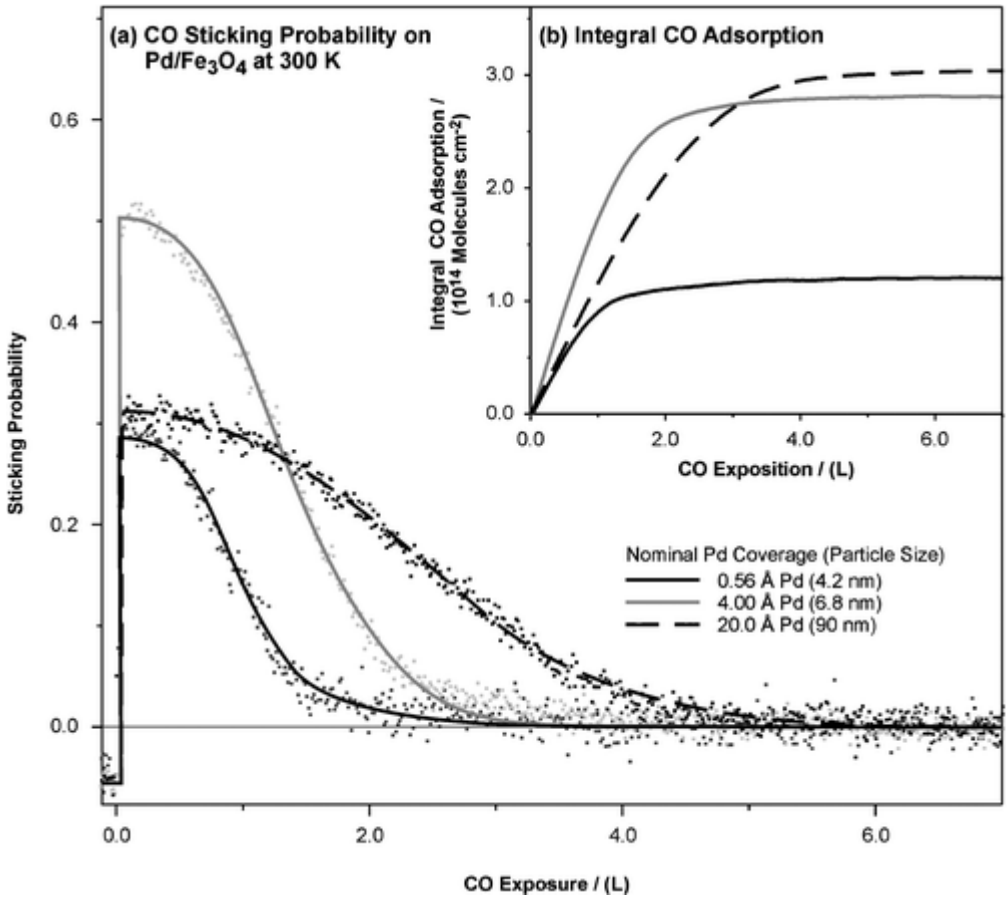

Fig. 7 Direct comparison of the shape of the sticking coefficient curves (a) and the integral absorption capacity (b) for small, intermediate sized and large Pd particles on Fe_3O_4.

This, at a first glance somewhat surprising behavior can be understood on the basis of a combination of the Pd growth and the so called "capture zone effect". The capture zone effect for supported catalysts was first formulated by Gillet and Matolin[70,71] and later experimentally investigated by many other authors (see *e.g.*ref. 32 and 72). Briefly, it is found that on supported particle systems two adsorption channels exist. In addition to the adsorbate molecules directly impinging on the active particles, other molecules may be trapped on the support and reach the particles *via* surface diffusion. The equivalent area from which impinging adsorbates can be collected by the particles, is termed the " capture zone". The effect may substantially enhance the adsorption rate on the particles and, provided that the adsorption process has some degree of rate control, may also have an effect on the kinetics of catalytic reactions.

Schematically, the effect of the capture zone as a function of particle size and density is depicted in Fig. 8. At low nominal Pd coverage, *i.e.* for small particles and not too high particle densities, the capture zones are not expected to overlap substantially. Consequently, the initial sticking coefficient increases with Pd coverage as a result of the increasing particle size and density. The exposure required for CO saturation increases with increasing Pd coverage, due to the rapidly increasing particle surface (which is not compensated for the moderately increasing sticking coefficient).

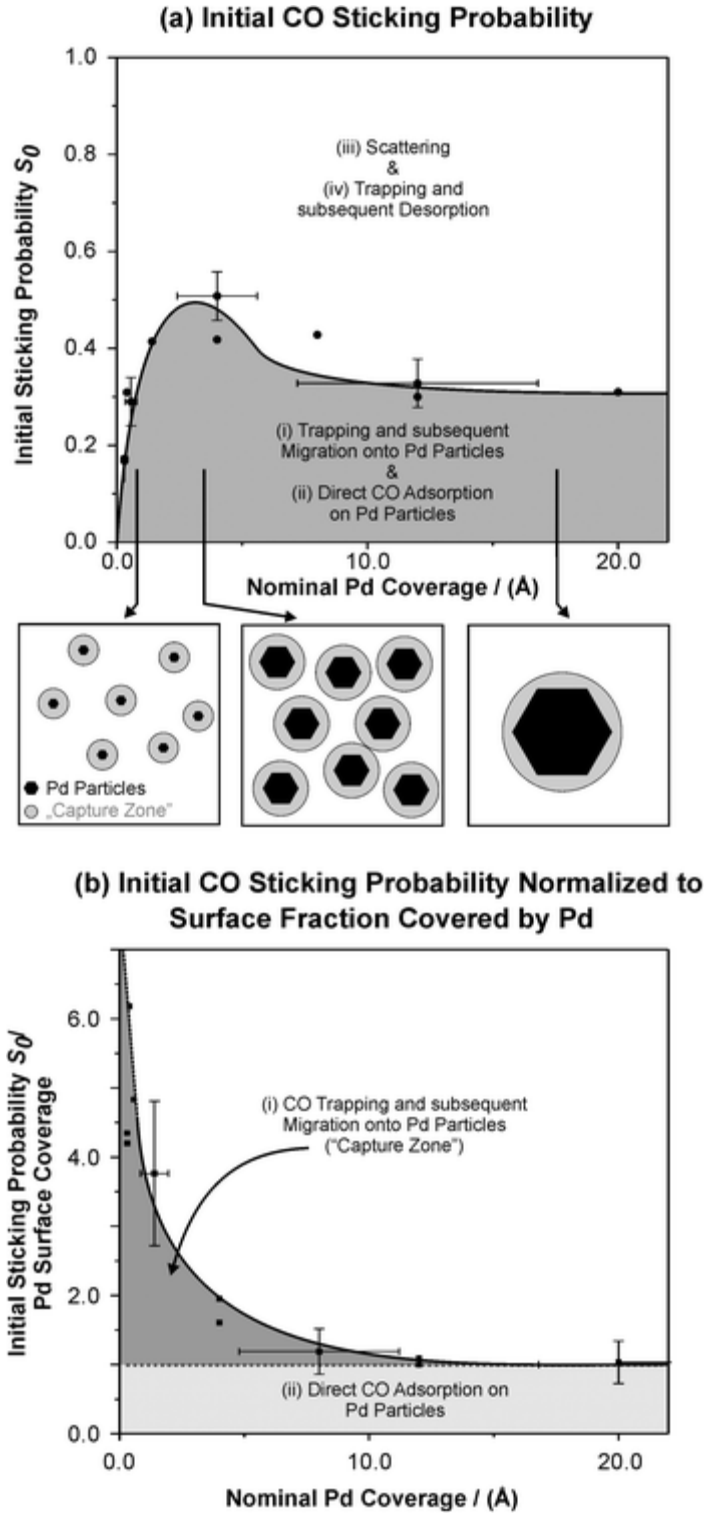

Fig. 8 (a) Initial sticking coefficient of CO on the Pd/Fe_3O_4 model catalyst at 300 K; (b) estimated contribution of the adsorption channels due to direct impingement on the Pd and due to trapping on the Fe_3O_4 support and diffusion to the Pd particles ("capture zone effect", see text).

If we now switch to high Pd coverage, we are dealing with very large Pd islands. Adsorption on these islands is expected to be dominated by direct impingement on the Pd islands, and the contribution of the capture zone should be small. As a result, the exposure required for CO saturation is even larger and approaches the single crystal value. The average distance between the Pd particles also increases for large nominal Pd coverage due to the low island density as illustrated in Fig. 8a (compare with section 3.1). As a result, the probability of CO molecules trapped on the support to be collected by the

particles decreases (because the width of the capture zone stays constant) and so does the initial sticking coefficient S_0.

In order to quantify the role of the capture zone effect we proceed as follows: we assume an initial sticking coefficient S_0 on the Pd particles close to unity, similar as observed for the single crystal surface (compare, *e.g.*, with ref. 69). Next, we estimate the fraction of the support covered by Pd on the basis of the STM-based model described in section 3.1. The enhancement of the adsorption rate due to the capture zone is given by the ratio of S_0 and the fraction of the Pd-covered support. The result is displayed in Fig. 8b. We find an enhancement factor of up to approximately 6 for the smallest particles. With increasing nominal Pd coverage the enhancement factor decreases monotonously. From this data, we can estimate the size of the capture zone as $\Delta R = 1.7 \pm 0.7$ nm. This value is comparable to the estimates by Matolin and coworkers, who calculated capture zones with ΔR between 0.5 and 3.3 nm for CO adsorption at 300 K on Pd particles supported on different types of α- and γ-Al_2O_3 surfaces.[73–75]

3.4 Size dependent oxygen adsorption and oxidation behavior

In the last part of this work, we discuss the oxygen adsorption and oxidation behavior of the Pd/Fe_3O_4 model catalyst. In the first step, we consider the dissociative adsorption of oxygen on metallic Pd only. In a previous work we have shown that at temperatures below 450 K oxygen predominantly chemisorbs dissociatively on the Pd particles.[6] We may assume that the Pd oxide formation is kinetically hindered in this temperature region under the conditions applied.[14,20]

In order to probe the oxygen adsorption capacity, a molecular beam CO titration experiment is performed (see Fig. 9). First, the sample is exposed to an extended pulse of O_2 (100 s), which leads to saturation of the Pd surface by chemisorbed oxygen. After a delay time of 10 s the surface is exposed to a pulse of CO (60 s). During the CO pulse, the CO_2 production is recorded. It is found that the initial CO_2 production rate first increases with increasing nominal Pd coverage whereas at high Pd coverage it shows a maximum and then decreases slightly.

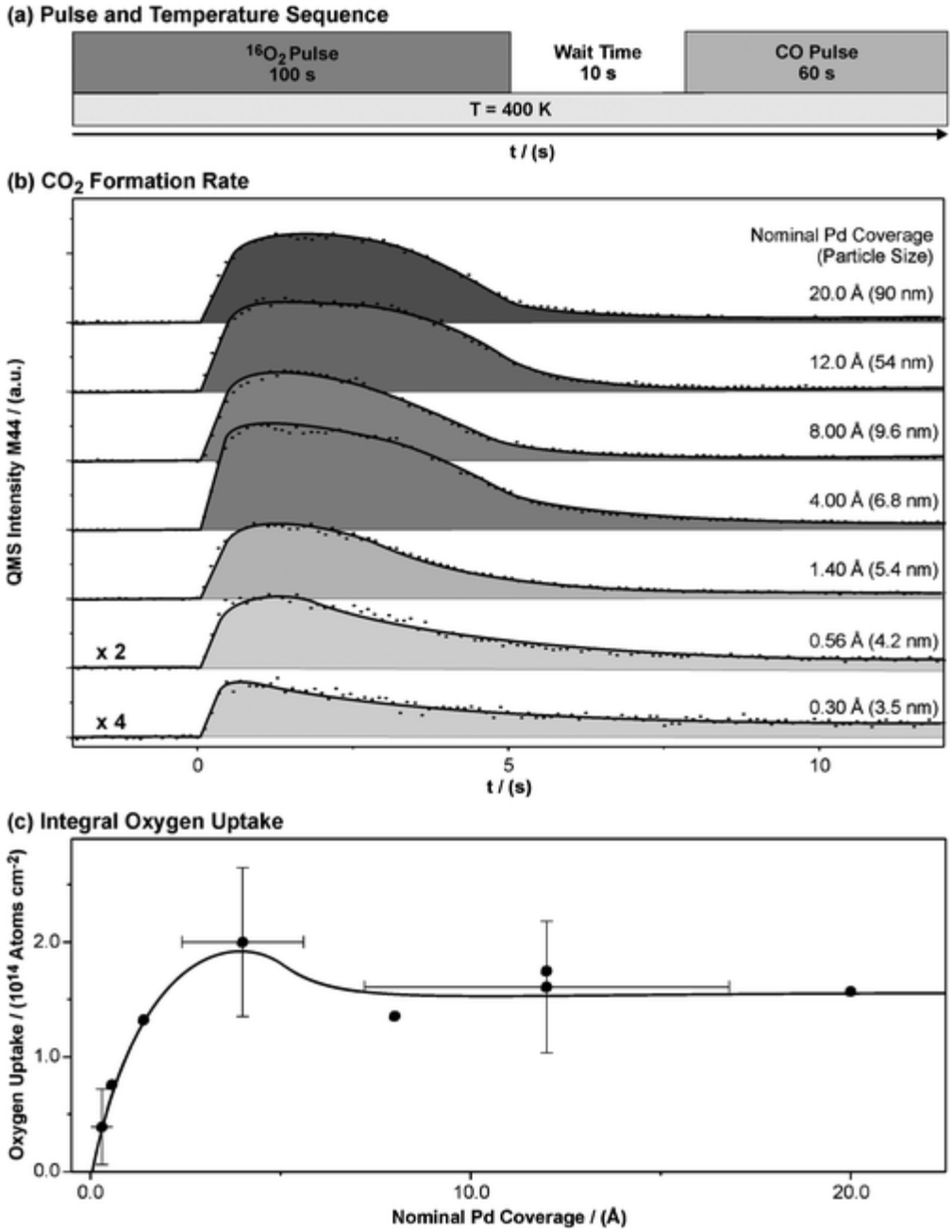

Fig. 9 Molecular beam CO titration experiments on an oxygen-precovered Pd/Fe_3O_4 model catalyst at 400 K.

Apparently, this behavior is similar to the Pd coverage dependence of the CO sticking coefficient. It can be easily explained if we consider that at high oxygen coverage CO adsorption is expected to be the rate determining step of the CO oxidation reaction. Consequently, the initial CO_2 production rate represents the CO sticking coefficient on the oxygen saturated surface. Apparently, CO adsorption on the oxygen saturated surface shows similar effects due to the capture zone as CO adsorption on the clean surface (see section 3.3).

In order to quantify the amount of adsorbed oxygen, we integrate over the complete CO_2 production. A corresponding plot is shown in Fig. 9c. The absolute oxygen uptake is estimated on the basis of the morphology of the Pd particles at a nominal Pd coverage of 4 Å (see section 3.1). On the basis of the ratio of (111) facets (80%) to (100) facets (20%) and the saturation coverage on the single crystal surfaces (Pd(111): $\theta_{CO} = 0.5$,[40,69] $\theta_O = 0.25$,[8] Pd(100): $\theta_{CO} = 0.5$,[40] $\theta_O = 0.5$[76]) the average saturation coverage on the particles are calculated as $\overline{\theta}_O = 0.3$ and $\overline{\theta}_{CO} = 0.5$. With the data in Fig. 6 we obtain an absolute oxygen uptake of 2×10^{14} atoms· cm^{-2} at a nominal Pd coverage of 4 Å. This value is consistent with oxygen sticking coefficient measurements on the Pd/Fe_3O_4 model catalyst

reported recently.[6]

It is found that the oxygen uptake as a function of the nominal Pd coverage follows a similar behavior as the CO adsorption capacity. At low Pd coverages the adsorption capacity increases rapidly, reaches a maximum at a nominal Pd coverage of about 4 Å and decreases slightly at higher coverage as a result of particle coalescence. Therefore we conclude that independently of the particle size oxygen chemisorption dominates on the metallic Pd particles at 400 K.

Next, we investigate the particle size dependent oxidation of the Pd particles at 500 K. In order to quantify the amount of Pd oxide formed, pulsed CO titration experiments are performed, which are schematically depicted in Fig. 10a.[25] The sample is exposed to a pulse of O_2 (100s) and, subsequently, 360 pulses of CO (5s on-time, 5s off-time) are applied. In comparison to a continuous beam experiment, the pulse experiment has the advantage that the CO_2 formation can be detected easily even at very low rates (see Fig. 10b). As discussed previously, the CO_2 formation kinetics shows a bimodal behavior:[23] fast initial CO_2 production during the first pulse can be attributed to reaction of CO with chemisorbed O on metallic Pd. Slow CO_2 production during the following pulses can be assigned to reduction of the surface and interface oxides. The total oxygen release is determined by integrating over 300 pulses after subtraction of the average signal of the last 60 pulses, used as a background signal. The results of these experiments are plotted in Fig. 11a (upper trace). An absolute calibration of the oxygen release is obtained by comparison with the integral CO_2 signal obtained from the CO titration experiment at 400 K in Fig. 9 (see Fig. 11a, lower trace).

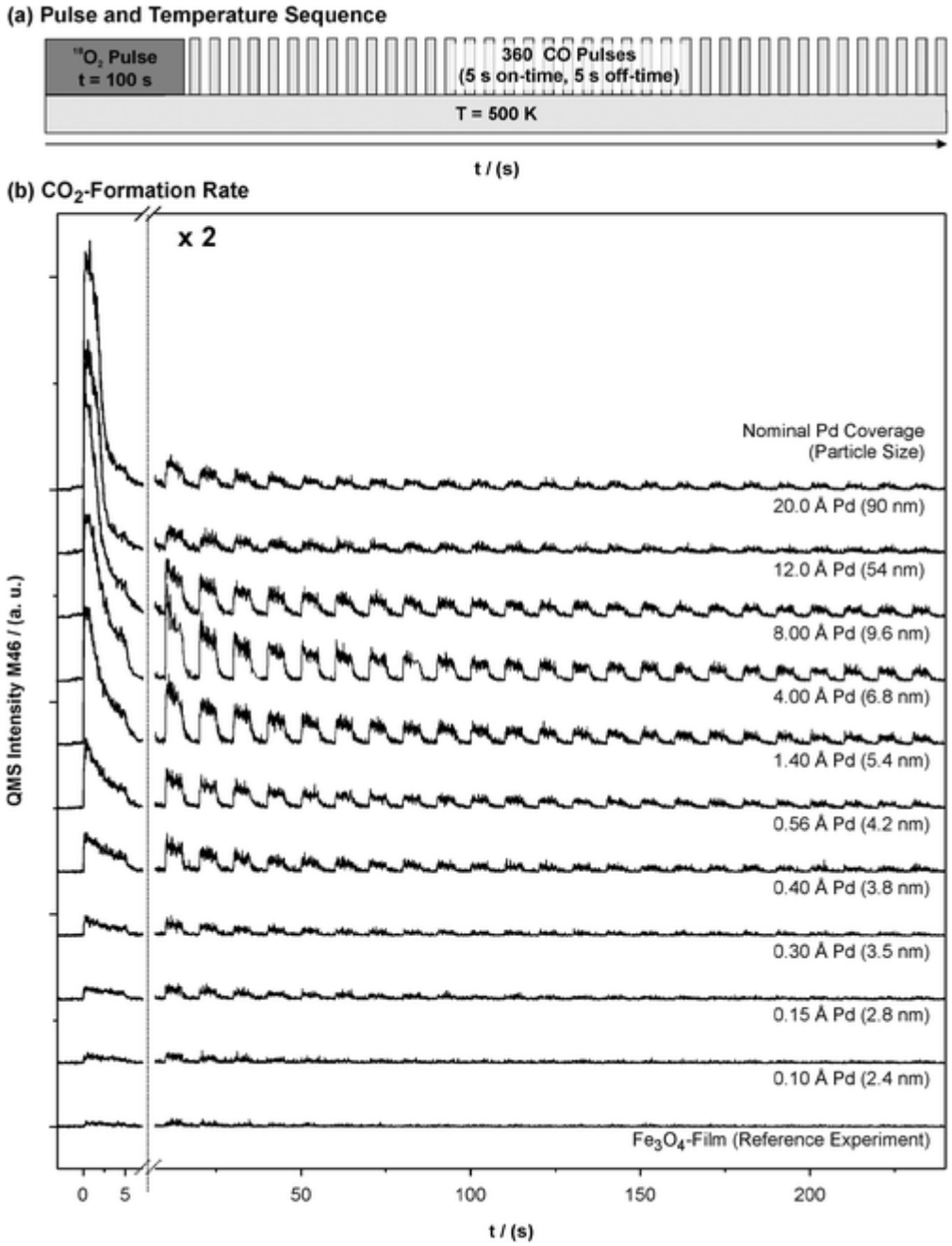

Fig. 10 Pulsed molecular beam CO titration experiments on partially oxidized and oxygen-precovered Pd particles on Fe_3O_4 at 500 K.

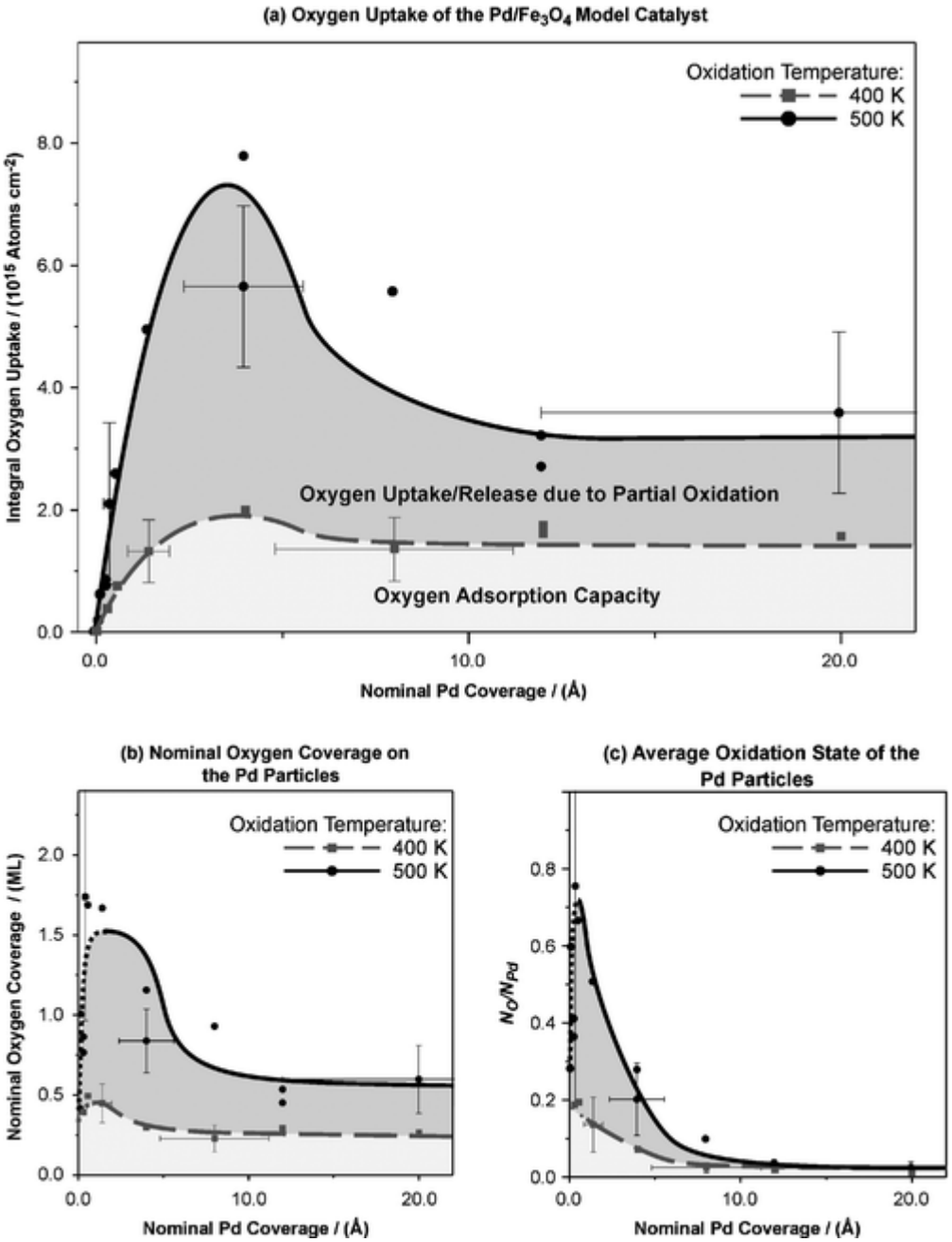

Fig. 11 Reversible oxygen uptake of the Pd/Fe_3O_4 model catalyst at 400 K (only chemisorption of oxygen) and at 500 K (chemisorption and oxide formation) as a function of nominal Pd coverage as determined from pulsed molecular beam titration experiments; (b) reversible oxygen uptake per Pd surface area; (c) reversible oxygen uptake per Pd atom deposited.

It is found that the total oxygen release initially increases with increasing nominal Pd coverage, shows a maximum at a Pd coverage around 4 Å and decreases rapidly at higher Pd coverages. This behavior cannot be explained on the basis of the total surface area of the Pd particles but points to a pronounced particle size dependence of the oxide formation. For small particles, kinetic hindrances are minor and the particles are easily oxidized under the conditions applied here. For larger particles, however, strong kinetic hindrances exist and surface or interface oxides are hardly formed. As a result, the oxygen release drops with increasing Pd coverage in spite of a nearly constant surface area. The region where this drop in oxygen release is observed coincides with the region of coalescence, in which the most rapid increase of particle size occurs (compare section 3.1). It should be noted that even for largest particle sizes the oxygen release at 500 K is significantly larger than at 400 K. This effect may

be associated with a small fraction of Pd oxide formation even on large particles.

In order to obtain more information on the oxide formation as a function of particle size, it is useful to relate the oxygen release to the number of Pd surface and bulk atoms. To calculate the number of oxygen atoms per Pd surface atom we estimate the surface area of the particles on the basis of the STM-based model discussed in section 3.1. The data is normalized such that the oxygen coverage for chemisorption (400 K) at a Pd coverage of 4 Å is $\theta_O = 0.3$ (see discussion above). The result is shown in Fig. 11b. We find that the oxygen release at 400 K (chemisorption only) remains constant within our experimental accuracy, whereas the oxygen release at 500 K (Pd oxidation and chemisorption) shows a step-like increase for nominal Pd coverages below 4 Å (corresponding to an average particle size around 7 nm). For smaller particles the ratio of oxygen to Pd surface atoms increases to a value of approximately 1.5. It is difficult to estimate the exact thickness of the surface and interface oxide from this number, as we have no detailed information on the distribution of the oxide over the Pd/Fe_3O_4 interface. We have to take into account that in addition to the Pd/Fe_3O_4 interface, a minor part of the outer surface of the Pd particles is also oxidized and the remaining metallic fraction is saturated with chemisorbed oxygen.[6] Taking all points into consideration it appears likely that the average thickness of the Pd surface and interface oxide on the Pd particles is thicker than the surface oxide on Pd(111) ($\theta_O = 0.7$, see ref. 18).

Finally, it is interesting to estimate the average oxidation state of the complete particles, by calculating the ratio between the oxygen uptake and the total amount of Pd deposited (see Fig. 11c). We find that with decreasing nominal Pd coverage the average oxidation state rapidly increases for Pd coverages of 4 Å and below (corresponding to an average particle size of 7 nm). For very small particles the oxygen release points to an O/Pd ratio of around 0.6 to 0.8.

One might assume that for very small particles, for which no substantial kinetic limitations with respect to oxidations exist, the stoichiometry may approach PdO. This assumption is not supported by the titration experiments, however. Instead the oxygen release appears to decrease again for the smallest particles. We have to treat this observation with care because of the large experimental uncertainties in the limit of small particles. Still, it is important to notice that a decreasing oxygen release for the smallest particles does not necessarily imply a hindered oxidation. Instead, it may also point to a hindered reduction upon CO exposure. Such an effect would be compatible with the anomalous CO adsorption behavior for very small particles (see section 3.2) which was tentatively assigned to a strong interaction with oxygen from the support or a partial oxidation of the Pd particles, remaining even after extended CO exposure.

4. Conclusions

We have investigated (i) the particle size dependence of CO and oxygen adsorption and (ii) the particle size dependence of oxidation of Pd nanoparticles using a supported Pd model catalyst based on an ordered Fe_3O_4 film on Pt(111).

(1) The morphology, nucleation, growth and coalescence behavior of the Pd particles immediately after preparation and after stabilization by thermal treatment in oxygen were characterized by STM. Pd particles in a size range between roughly 1 and 100 nm could be prepared.

(2) The morphological changes as a function of particle size can be monitored *via* IRAS (IR reflection absorption spectroscopy) of adsorbed CO as a probe molecule. Smaller particles show characteristic bands (125 K) due to on-top CO, the bands in the bridge- and hollow-regions show characteristic changes as a function of particle size and can be interpreted on the basis of single-crystal data.

(3) Very small Pd particles on Fe_3O_4 show an anomalous adsorption behavior, which is characterized by weak CO adsorption and a CO stretching frequency in the range of 2130 cm^{-1}. This modified adsorption behavior is attributed to the interaction of small Pd particles with the support.

(4) The CO adsorption kinetics shows a strong enhancement due to trapping and diffusion on the support (capture zone effect). The capture zone is quantified on the basis of structural data from STM. In the limit of small particles the CO adsorption rate is enhanced by up to a factor of 6 (300 K). The enhancement effect becomes negligible for very large particles.

(5) Oxygen adsorption at 400 K was quantified by means of CO titration experiments and shows a

size dependent behavior similar to CO adsorption. This observation suggests that independently of the particle size oxygen adsorbs dissociatively at 400 K and almost no Pd oxidation occurs.

(6) Oxidation and reduction of the Pd particle was investigated as a function of particle size at 500 K. Interface oxidation and partial surface oxidation occur easily at particle sizes up to approximately 7 nm. On larger particles strong kinetic hindrances with respect to oxidation are observed. On the contrary, smaller particles are easily oxidized. Estimates point to the formation of oxide layers which, in average, are thicker than the surface oxides formed on single crystal surfaces. Full reduction of very small Pd particles may be hindered due to strong interaction with the support.

Acknowledgements

This work has been funded by the Deutsche Forschungsgemeinschaft (SPP 1091) and the Fonds der Chemischen Industrie.

References

1 G. Ertl, H. Knoezinger and J. Weitkamp, in *Handbook of Heterogeneous Catalysis*, ed. G. Ertl, H. Knoezinger and J. Weitkamp, VCH, Weinheim, 1997.

2 J. M. Thomas and W. J. Thomas, *Principle and Practice of Heterogeneous Catalysis*, VCH, Weinheim, 1997.

3 H. Over, Y. D. Kim, A. P. Seitsonen, S. Wendt, E. Lundgren, M. Schmid, P. Varga, A. Morgante and G. Ertl, *Science*, 2000, **287**, 1474 [Links].

4 J. Klikovits, M. Schmid, J. Gustafson, J. Mikkelsen, A. Resta, E. Lundgren, J. N. Andersen and P. Varga, *J. Phys. Chem. B*, 2006, **110**, 9966 [Links].

5 B. L. M. Hendriksen, S. C. Bobaru and J. W. M. Frenken, *Top. Catal.*, 2005, **36**, 43 [Links].

6 T. Schalow, B. Brandt, M. Laurin, S. Guimond, H. Kuhlenbeck, S. Schauermann, J. Libuda and H.-J. Freund, *Surf. Sci.*, 2006, **600**, 2528 [Links].

7 T. Schalow, B. Brandt, M. Laurin, S. Schauermann, J. Libuda and H.-J. Freund, *J. Catal.*, 2006, **242**, 58 [Links].

8 H. Conrad, G. Ertl, J. Küppers and E. E. Latta, *Surf. Sci.*, 1977, **65**, 245 [Links].

9 R. Imbihl and J. E. Demuth, *Surf. Sci.*, 1986, **173**, 395 [Links].

10 S.-L. Chang and P. A. Thiel, *J. Chem. Phys.*, 1988, **88**, 2071 [Links].

11 X. Guo, A. Hoffman and J. T. Yates, Jr, *J. Chem. Phys.*, 1989, **90**, 5787 [Links].

12 V. A. Bondzie, P. Kleban and D. J. Dwyer, *Surf. Sci.*, 1996, **347**, 319 [Links].

13 E. H. Voogt, A. J. M. Mens and J. W. G. O. L. J. Gijzeman, *Surf. Sci.*, 1997, **373**, 210 [Links].

14 F. P. Leisenberger, G. Koller, M. Sock, S. Surnev, M. G. Ramsey, F. P. Netzer, B. Klötzer and K. Hayek, *Surf. Sci.*, 2000, **445**, 380 [Links].

15 V. A. Bondzie, P. H. Kleban and D. J. Dwyer, *Surf. Sci.*, 2000, **465**, 266 [Links].

16 G. Zheng and E. I. Altman, *Surf. Sci.*, 2000, **462**, 151 [Links].

17 G. Zheng and E. I. Altman, *Surf. Sci.*, 2002, **504**, 253 [Links].

18 E. Lundgren, G. Kresse, C. Klein, M. Borg, J. N. Andersen, M. De Santis, Y. Gauthier, C. Konvicka, M. Schmid and P. Varga, *Phys. Rev. Lett.*, 2002, **88**, 246103 [Links].

19 M. Todorova, E. Lundgren, V. Blum, A. Mikkelsen, S. Gray, J. Gustafson, M. Borg, J. Rogal, K. Reuter, J. N. Andersen and M. Scheffler, *Surf. Sci.*, 2003, **541**, 101 [Links].

20 E. Lundgren, J. Gustafson, A. Mikkelsen, J. N. Andersen, A. Stierle, H. Dosch, M. Todorova, J. Rogal, K. Reuter and M. Scheffler, *Phys. Rev. Lett.*, 2004, **92**, 046101 [Links].

21 M. Todorova, K. Reuter and M. Scheffler, *Phys. Rev. B: Condens. Matter*, 2005, **71**, 195403 [Links].

22 A. Stierle, N. Kasper, H. Dosch, E. Lundgren, J. Gustafson, A. Mikkelsen and J. N. Andersen, *J. Chem. Phys.*, 2005, **122**, 44706 [Links].

23 T. Schalow, M. Laurin, B. Brandt, S. Schauermann, S. Guimond, H. Kuhlenbeck, D. E. Starr, S. k. Shaikhutdinov, J. Libuda and H.-J. Freund, *Angew. Chem., Int. Ed.*, 2005, **44**, 7601 [Links].

24 T. Schalow, B. Brandt, D. E. Starr, M. Laurin, S. Schauermann, S. K. Shaikhutdinov, J. Libuda and H.-J. Freund, *Catal. Lett.*, 2006, **107**, 189 [Links].

25 T. Schalow, B. Brandt, D. E. Starr, M. Laurin, S. K. Shaikhutdinov, S. Schauermann, J. Libuda and H.-J. Freund, *Angew. Chem., Int. Ed.*, 2006, **45**, 3775 [Links].

26 N. Kasper, A. Stierle, P. Nolte, Y. Jin-Phillipp, T. Wagner, D. G. d. Oteyza and H. Dosch, *Surf. Sci.*, 2006, **600**, 2860 [Links].

27 B. L. M. Hendriksen, S. C. Bobaru and J. W. M. Frenken, *Surf. Sci.*, 2004, **552**, 229 [Links].

28 G. Zheng and E. I. Altmann, *J. Phys. Chem. B*, 2002, **2002**, 1048 [Links].

29 M. P. D'Evelyn and R. J. Madix, *Surf. Sci. Rep.*, 1984, **3**, 413 [Links].

30 M. Asscher and G. A. Somorjai, in *Atomic and Molecular Beam Methods*, ed. G. Scoles, Oxford University Press, 1988, vol. 2, p. 489.

31 A. W. Kleyn, *Chem. Soc. Rev.*, 2003, **32**, 87 [Links].

32 J. Libuda and H.-J. Freund, *Surf. Sci. Rep.*, 2005, **57**, 157 [Links].

33 J. Libuda, *Surf. Sci.*, 2005, **587**, 55 [Links].

34 J. Libuda, I. Meusel, J. Hartmann and H.-J. Freund, *Rev. Sci. Instrum.*, 2000, **71**, 4395 [Links].

35 W. Weiss and W. Ranke, *Prog. Surf. Sci.*, 2002, **70**, 1 [Links].

36 C. Lemire, R. Meyer, V. Henrich, S. K. Shaikhutdinov and H.-J. Freund, *Surf. Sci.*, 2004, **572**, 103 [Links].

37 M. Bäumer and H.-J. Freund, *Prog. Surf. Sci.*, 1999, **61**, 127 [Links].

38 K. H. Hansen, T. Worren, S. Stempel, E. Laegsgaard, M. Bäumer, H.-J. Freund, F. Besenbacher and I. Stensgaard, *Phys. Rev. Lett.*, 1999, **83**, 4120 [Links].

39 H. Graoui, S. Giorgio and C. R. Henry, *Surf. Sci.*, 1998, **417**, 350 [Links].

40 A. M. Bradshaw and F. M. Hoffman, *Surf. Sci.*, 1978, **72**, 513 [Links].

41 F. M. Hoffmann, *Surf. Sci. Rep.*, 1983, **3**, 107 [Links].

42 H. Ohtani, M. A. van Hove and G. Sormorjai, *Surf. Sci.*, 1987, **187**, 372 [Links].

43 W. K. Kuhn, J. Szanyi and D. W. Goodman, *Surf. Sci.*, 1992, **274**, L611 [Links].

44 T. Gießel, O. Schaff, C. J. Hirschmugl, V. Fernandez, K.-M. Schindler, A. Theobald, S. Bao, R. Lindsay, W. Berndt, A. M. Bradshaw, C. Baddeley, A. F. Lee, R. M. Lambert and D. P. Woodruff, *Surf. Sci.*, 1998, **406**, 90 [Links].

45 D. Loffreda, D. Simon and P. Sautet, *Surf. Sci.*, 1999, **425**, 68 [Links].

46 L. Surnev, M. Sock, M. G. Ramsey, F. P. Netzer, M. Wiklund, A. Borg and J. N. Andersen, *Surf. Sci.*, 2000, **470**, 171 [Links].

47 M. K. Rose, T. Mitsui, J. C. Dunphy, A. Borg, D. F. Ogletree, M. Salmeron and P. Sautet, *Surf. Sci.*, 2002, **512**, 48 [Links].

48 M. Tüshaus, PhD thesis, Freie Universität Berlin, Berlin, 1990.

49 M. Tüshaus, W. Berndt, H. Conrad, A. M. Bradshaw and B. Persson, *Appl. Phys. A: Mater. Sci. Process.*, 1990, **51**, 91 [Links].

50 G. Rupprechter, *Phys. Chem. Chem. Phys.*, 2001, **3**, 4621 [Links].

51 H. Unterhalt, G. Rupprechter and H.-J. Freund, *J. Phys. Chem. B*, 2002, **109**, 502.

52 A. Ortega, F. M. Hoffman and A. M. Bradshaw, *Surf. Sci.*, 1982, **119**, 79 [Links].

53 K. Wolter, O. Seiferth, J. Libuda, H. Kuhlenbeck, M. Bäumer and H.-J. Freund, *Surf. Sci.*, 1998, **402–404**, 428 [Links].

54 A. Sandell, J. Libuda, P. A. Brühwiler, S. Andersson, M. Bäumer, A. J. Maxwell, N. Mårtensson and H.-J. Freund, *Phys. Rev. B: Condens. Matter*, 1997, **55**, 7233 [Links].

55 A. Sandell, A. Beutler, R. Nyholm, J. N. Andersson, P. A. Brühwiler, N. Martensson, J. Libuda, K. Wolter, O. Seiferth, M. Bäumer, H. Kuhlenbeck and H.-J. Freund, *Phys. Rev. B: Condens. Matter*, 1998, **57**, 13199 [Links].

56 I. Meusel, J. Hoffmann, J. Hartmann, J. Libuda and H.-J. Freund, *J. Phys. Chem. B*, 2001, **105**, 3567 [Links].

57 M. Frank and M. Bäumer, *Phys. Chem. Chem. Phys.*, 2000, **2**, 3723 [Links].

58 I. V. Yudanov, R. Sahnoun, K. M. Neyman, N. Rösch, J. Hoffmann, S. Schauermann, V. Johánek, H. Unterhalt, G. Rupprechter, J. Libuda and H.-J. Freund, *J. Phys. Chem. B*, 2003, **107**, 255 [Links].

59 P. Hollins, *Surf. Sci. Rep.*, 1992, **16**, 51 [Links].

60 Y. Chabal, *Surf. Sci. Rep.*, 1988, **8**, 211 [Links].

61 X. Xu and D. W. Goodman, *J. Phys. Chem.*, 1993, **97**, 7711 [Links].

62 A. Sandell, J. Libuda, P. A. Brühwiler, S. Andersson, A. J. Maxwell, M. Bäumer, N. Mårtensson and H.-J. Freund, *J. Vac. Sci. Technol., A*, 1996, **14**, 1546 [Links].

63 S. Shaikhutdinov, M. Heemeier, J. Hoffmann, I. Meusel, B. Richter, M. Bäumer, H. Kuhlenbeck, J. Libuda, H.-J. Freund, R. Oldman, S. D. Jackson, C. Konvicka, M. Schmid and P. Varga, *Surf. Sci.*, 2002, **501**, 270 [Links].

64 C. Duriez, C. R. Henry and C. Chapon, *Surf. Sci.*, 1991, **253**, 190 [Links].

65 C. R. Henry, C. Chapon, C. Goyhenex and R. Monot, *Surf. Sci.*, 1992, **272**, 283 [Links].

66 C. R. Henry, C. Chapon and C. Duriez, *Z. Phys. D*, 1991, **19**, 347 [Links].

67 D. A. King and M. G. Wells, *Surf. Sci.*, 1972, **29**, 454 [Links].

68 D. A. King and M. G. Wells, *Proc. R. Soc. London, Ser. A*, 1974, **339**, 245 [Links].

69 T. Engel, *J. Chem. Phys.*, 1978, **69**, 373 [Links].

70 E. Gillet, S. Channakhone, V. Matolin and M. Gillet, *Surf. Sci.*, 1985, **152/153**, 603 [Links].

71 V. Matolin and E. Gillet, *Surf. Sci.*, 1986, **166**, L115 [Links].

72 C. R. Henry, *Surf. Sci. Rep.*, 1998, **31**, 231 [Links].

73 I. Stara, V. Nehasil and V. Matolin, *Surf. Sci.*, 1996, **365**, 69 [Links].

74 I. Stara and V. Matolin, *Surf. Rev. Lett.*, 1997, **4**, 1353 [Links].

75 I. Jungwirthova, I. Stara and V. Matolin, *Surf. Sci.*, 1997, **377**, 644 [Links].

76 T. W. Orent and S. D. Bader, *Surf. Sci.*, 1982, **115**, 323 [Links].

Footnotes

† The HTML version of this article has been enhanced with colour images.

‡ Lehrstuhl für Physikalische Chemie II, Universität Erlangen-Nürnberg, Egerlandstr. 3, D-91058 Erlangen, Germany. E-mail: E-mail: joerg.libuda@chemie.uni-erlangen.de.